ChemCatChem

Research Article
doi.org/10.1002/cctc.202201470

Chemistry Europe
European Chemical Societies Publishing

www.chemcatchem.org

VIP *Very Important Paper*

IrO_2/Ir Composite Nanoparticles (IrO_2@Ir) Supported on TiN_xO_y Coated TiN: Efficient and Robust Oxygen Evolution Reaction Catalyst for Water Electrolysis

Swapnil Sanjay Karade,[a] Raghunandan Sharma,*[a] Saso Gyergyek,[b] Per Morgen,[a] and Shuang Ma Andersen*[a]

It is crucial but challenging to reduce the required noble-metal loading without compromising the catalytic performance of oxygen evolution reaction (OER) catalysts. This study presents a highly active OER catalyst composed of IrO_2 with Ir rich surface (IrO_2@Ir) nanoparticles supported over nano TiN coated with TiO_xN_y (IrO_2@Ir/TiN). The present approach demonstrates superior OER catalysts with high activity through small, uniformly dispersed IrO_2@Ir nanoparticles, along with high durability owing to robust catalyst support and strong catalyst-support interaction. The synthesized IrO_2@Ir/TiN with an Ir loading of 40 wt% exhibits a mass-normalized OER activity of 637 $A g_{Ir}^{-1}$, which is 2.4 times that of the unsupported commercial benchmark IrO_2 OER electrocatalyst. The fine nanoparticles and high activity enable significant (~60%) reduction in the Ir metal loading required to obtain equivalent OER performance. In addition, when evaluated through an accelerated stress test using potential cycling, the catalyst exhibits outstanding durability (79% retention) compared to that of the commercial equivalent (66% retention). The OER activity loss was attributed to the catalyst dissolution (30% loss) and the catalyst particle growth (70%), with no measurable loss due to the TiN support corrosion. The development of ultra-fine IrO_2@Ir nanoparticles and robust ceramic catalyst support significantly improved the Ir utilization and open a new perspective for supported OER catalyst.

Introduction

When paired with renewable energy sources including solar, wind, and hydroelectric power, solid polymer electrolyte (SPE) water electrolysis is seen as a highly competitive technology for green hydrogen production.[1–6] To drive the oxygen evolution reaction (OER), water electrolysis requires efficient and stable catalysts, and the best ones found till date to meet these requirements are based on Ir.[7–9] However, these catalysts, owing to low abundance of Ir in the upper earth crust, are highly expensive, which limits further market expansion of the SPE water electrolyzers (SPEWEs).[10,11] As a result, a crucial need for large-scale applicability of the SPEWE approach is to reduce the required quantity of noble metals per unit of the generated hydrogen.[12,13] An effective strategy to deal with this issue could be to increase the mass specific activity of the catalyst by, for example, (i) increasing the effective surface to volume ratio, (ii) reduction of the kinetic overpotential by structural modifications of the active sites, etc. The effective surface area of the Ir-based catalysts may be enhanced by, for example, reducing the catalyst particle size and/or minimizing the particle agglomeration. This may be achieved through use of a catalyst support providing sites for heterogeneous nucleation during synthesis and preventing agglomeration of the catalyst particles through catalyst-support interaction. Hence, a supported catalyst can reduce the amount of the noble metals required to achieve certain catalytic activity by increasing their utilization. In addition, the catalyst-support interaction may engineer the d-band electronic energy states,[14,15] leading to enhanced catalytic activity and durability.

Characteristics of typical catalyst supports include high electrical conductivity, high surface area as well as high corrosion resistance.[16,17] In the harsh oxidative conditions (acidic environment and oxidative potentials) at the SPEWE anode, the high surface area carbon materials, which are typically employed as supports in fuel cells, are susceptible to corrosion.[18,19] Several acid-resistant semiconductive metal oxides and carbides have been explored to date for their suitability as the OER catalyst supports. Among those, metal oxides such as TiO_2 and SnO_2, despite their excellent corrosion resistance, have limited applicability as catalyst support due to their low electrical conductivity. Nonstoichiometric Ti/Ti-alloy oxides have been described in attempt to address the conductivity challenge. Such supports show significant enhancements in the mass specific OER activities of the Ir-based

[a] Dr. S. S. Karade, Prof. Dr. R. Sharma, Prof. Em. Dr. P. Morgen, Prof. Dr. S. M. Andersen
Department of Green Technology
University of Southern Denmark
M 5230 Odense (Denmark)
E-mail: rash@igt.sdu.dk
mashu@igt.sdu.dk
[b] Prof. Dr. S. Gyergyek
Department for Materials Synthesis
Jozef Stefan Institute
Jamova 39, SI-1000 Ljubljana (Slovenia)

Supporting information for this article is available on the WWW under https://doi.org/10.1002/cctc.202201470

catalysts. For example, Wang et al.[20] have reported excellent OER activity of Ir/Ti_4O_7 catalyst consisting of the nanostructured Ir loaded on the Ti_4O_7 suboxide substrate. Similarly, IrO_2 supported on $Nb_{0.05}Ti_{0.95}O_2$ showed a two-fold enhancement in the mass activity for OER compared to that of the unsupported equivalent.[21] Similarly, metal oxides such as antimony doped tin oxide (ATO),[22] Sb-SnO_2 nanowires,[23] etc. have also been reported to successfully enhance the mass activity of Ir-based OER catalysts. Apart from the metal oxides, metal carbides such as TiC, TaC, and SiC have also been reported as the support materials for OER.[24–29] However, despite significant research, their stability remains a challenge before such supported OER catalysts may be implemented at large-scale. Lower surface area and complex preparation methods also limit the large-scale use of as such supports.[25–28]

Although majority of the recent research on OER catalytic supports is on metal oxides and carbides, other candidates such as metal nitrides, owing to their typically high electric conductivity and high corrosion resistance, are equally interesting. As an example, titanium nitride (TiN) exhibits excellent electrical conductivity (resistivity of TiN: $3.34\times10^{-7}\,\Omega\,cm$ at room temperature, which is lower than that of metallic Ti: $5\times10^{-6}\,\Omega\,cm$), along with high resistance to oxidation and inertia to majority of the chemicals.[30,31] It has also been reported to be an effective electronic structure modulator, making it a promising support material for OER catalysts. Catalysts consisting of the Pt nanoparticles/Pt single atoms on TiN have also been reported frequently for reactions such as methanol oxidation and others.[30–35] Studies on TiN as a support for Pt-based catalysts for the oxygen reduction reaction (ORR) suggest TiN to be promising catalyst support for ORR electrocatalysis.[36] However, use of TiN as a support for the OER catalysts has rarely been explored. Recent studies by Li et al.[37] and Zhang et al.[38] have demonstrated the use of TiN as the catalyst support for Ir and/or IrO_2-based catalysts for OER, showing high activity and enhanced stability, which were attributed to the support/catalyst interaction leading to electron transfer from TiN to Ir, downshifting its d-band. Owing to their superior performance, the TiN supported Ir-based OER catalysts are promising candidates for large-scale applications and hence, their green and scalable synthesis routes need to be explored. Further understanding of the activity and durability enhancement mechanisms in presence of TiN may be used to obtain even higher performance electrocatalysts.

On the other hand, not only the bulk structure, but the surface chemical state of the catalyst support also plays significant role in the catalyst stability. In our previous study on carbon supported Pt (Pt/C), it has been observed that the presence of surface functional groups on the carbon support enhances the stability of the Pt/C electrocatalysts significantly. Similar effect of the presence of surface functionalities may be expected for the OER electrocatalysts. However, the effect has not been explored for the OER electrocatalysts supported on TiN.

Herein, we adopt a high throughput microwave assisted polyol method for the decoration of IrO_2@Ir nanoparticles on the nano-sized TiN support and study the electrocatalytic performance of the synthesized IrO_2@Ir/TiN towards the OER in acidic environment. We further carried out investigations on the effect of presence of TiO_xN_y on the performance of the electrocatalysts. Finally, study of the interaction between the TiN@TiO_xN_y support and the deposited Ir-based catalyst was performed and a mechanistic study of the catalyst degradation during an accelerated stress test (AST) was carried out by utilizing X-ray fluorescence (XRF) spectroscopy to measure the loss of catalyst loading from the electrode during AST.

Results and Discussion

Initial electrocatalytic OER activity: The OER catalytic performance of synthesized IrO_2@Ir/TiN catalysts with different compositions were assessed using a polarization test in N_2-saturated 0.1 M $HClO_4$ electrolyte at a 1600 rpm electrode rotation speed. Figure 1a shows OER polarization curves corresponding to all compositions of the Ir/TiN, where commercial IrO_2 catalyst (Alfa Aesar) was used as a standard benchmark. Almost all the supported catalysts showed superior performance as compared to the unsupported commercial IrO_2. Among the studied compositions, IrO_2@Ir/TiN-40 demonstrates the highest mass specific activity, ~2.4 times that of the benchmark IrO_2 catalyst (Figure 1b). The mass specific activity of the supported catalysts increases with increasing the Ir loading from 20 wt% to 40 wt%, while decreases with further increasing the Ir loading from 40 wt% to 80 wt%. This may be explained in terms of utilization of the OER active species loaded on the support. For low IrO_2@Ir loading (20 wt%), the utilization is low possibly due to (i) the deposition of fraction of the IrO_2@Ir nanoparticles in pores, which remain inaccessible for the electrolyte and (ii) the poor electric conductivity of the support, leading to inefficient electronic connectivity. With increasing IrO_2@Ir loading, the electric conduction may take place (partially) through the quasi-continuous IrO_2@Ir coating, leading to improved electronic connectivity. Further increase of the Ir loading (50 wt% to 80 wt%) the utilization of the OER active surface decreases due to formation of IrO_2@Ir agglomerates, effectively obscuring the active surface partially by other IrO_2@Ir nanoparticles. Hence, the Ir loading of 40 wt% shows the highest mass specific activity.

Further, it is observed that variation of the Ir loading also affects the intrinsic OER activity in terms of the reaction overpotential (η), defined as- $\eta = E_{Onset} - E_O$, where E_{Onset} and E_O are the OER onset potential and the standard reduction potential for OER ($E_O = 1.23$ V at 0 pH), respectively. Figure 1c depicts the reaction overpotential obtained for the studied catalysts. It reveals significantly lower overpotential for IrO_2@Ir/TiN-40 sample as compared to the commercial IrO_2 benchmark. Tafel plots fitted from OER polarization curves were used to examine the reaction kinetics (Figure 1d). Among all the examined samples, the IrO_2@Ir/TiN-40 electrode shows the smallest Tafel slope of 63.3 mV dec^{-1}, indicating the most favorable OER kinetics.

Morphology and composition of as-synthesized IrO_2@Ir/TiN: The synthesized electrocatalyst having the highest OER mass

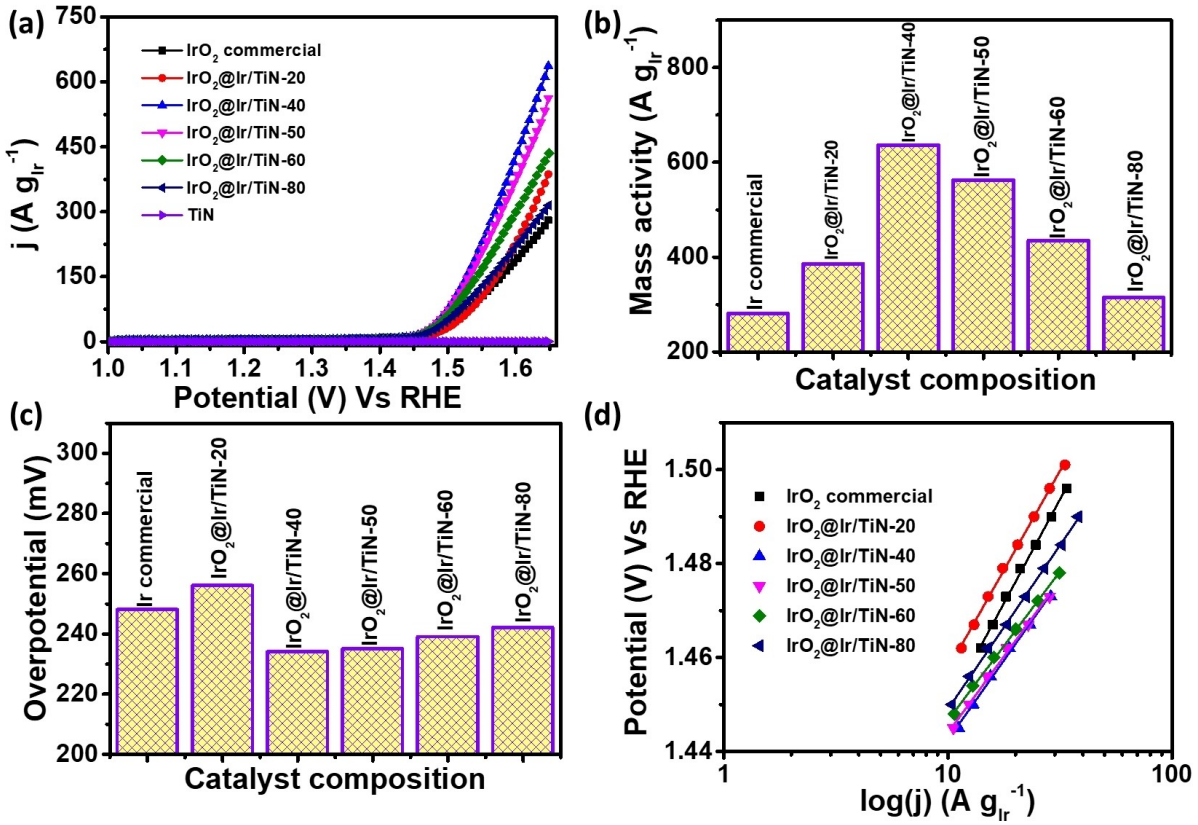

Figure 1. (a) OER polarization curves for as-prepared IrO_2@Ir/TiN based catalysts with reference to commercial IrO_2, bar plot of (b) mass activity and (c) overpotential for different catalyst compositions, (d) corresponding Tafel plot.

activity, i.e., IrO_2@Ir/TiN-40 and the TiN-AT used as the catalyst support were further analyzed through different structural characterization techniques.

TEM was used to examine the differences between two samples in greater detail. TiN was made up of random-shaped nanoparticles of an average diameter 28 nm (Figure 2a). The diffraction rings and spots depicted in the selected area electron diffraction (SAED) image of TiN (Figure 2a, inset) reveal its crystalline nature. After the catalyst synthesis step, nano-sized TiN was ornamented by many uniformly dispersed IrO_2@Ir nanodots (IrO_2@Ir/TiN-40) with an average size of 2±0.2 nm (Figure 2b–d). The particle size distribution histograms (Supporting Information S1) reveal no morphological change of the TiN nanoparticles before and after IrO_2@Ir coting, confirming their chemical inertness under the synthesis conditions. The IrO_2@Ir nanodots of a particle size 2 nm, decorated over nano-sized TiN support, are clearly visible in TEM image (Figure 2c). SAED image (inset of Figure 2c) pertains to high crystalline nature of TiN similar with bare TiN (inset of Figure 2a) while no reflection of Ir and IrO_2 are seen due to their small size. The elemental contribution was analyzed further using EDS analysis (inset of Figure 2b), which confirms present IrO_2@Ir/TiN-40 sample contains Ti, N, Ir and O elements (contribution of carbon signal is due to conducting tape where the sample was loaded).

XRD patterns of the as prepared IrO_2@Ir/TiN catalysts recorded at 0.02 step size with 3°/min scan speed in the range of 10 to 90° are shown in Figure 3a. No obvious diffraction peaks corresponding to Ir or IrO_2 are observed, which implies an amorphous nature of the Ir based nanoparticles supported on nano-sized TiN. All the observed XRD peaks correspond to the TiN support (JCPDS: 038-1420).[40] The XRD pattern of commercial IrO_2 sample shows diffraction peaks at 41.0°, 47.5°, 69.6°, and 84.1°, which correspond respectively to the (111), (200), (220) and (311) planes of metallic Ir (JCPDS: 001-1212).

Surface chemical state and catalyst-support interaction: The chemical states and near-surface chemical compositions of the Ti, N, and Ir elements in as-received TiN, acid-treated TiN, and IrO_2@Ir/TiN-40 samples are evaluated using XPS. In the survey spectra of the as-received and acid-treated TiN, Ti 2p (457.4 eV), Ti 2s (556.0 eV), N 1s (389.1 eV), O 1s (530.2 eV), and C 1s (283.8 eV) peaks are observed (Figure 3b). Noticeable changes in surface composition of N 1s, C 1s and O 1s are observed after acid treatment, implying TiN surface being mostly free from the C and O species. Moreover, improved intensities of the N 1s and Ti 2p peaks on the acid-treated surface, corresponding to increased concentrations, may provide better conductive support and possible nucleation sites for the catalyst nanoparticle attachment. Likewise, the XPS survey spectrum of the IrO_2@Ir/TiN-40 sample exhibits presence of the Ir 4f (62.1 eV) and Ir 4p (493.2 eV) peaks along with the N 1s and Ti 2p peaks of reduced intensities comparing to the bare TiN support. Deconvolution of Ir 4f, Ti 2p, N 1s, and O 1s peaks of the narrow scan spectra

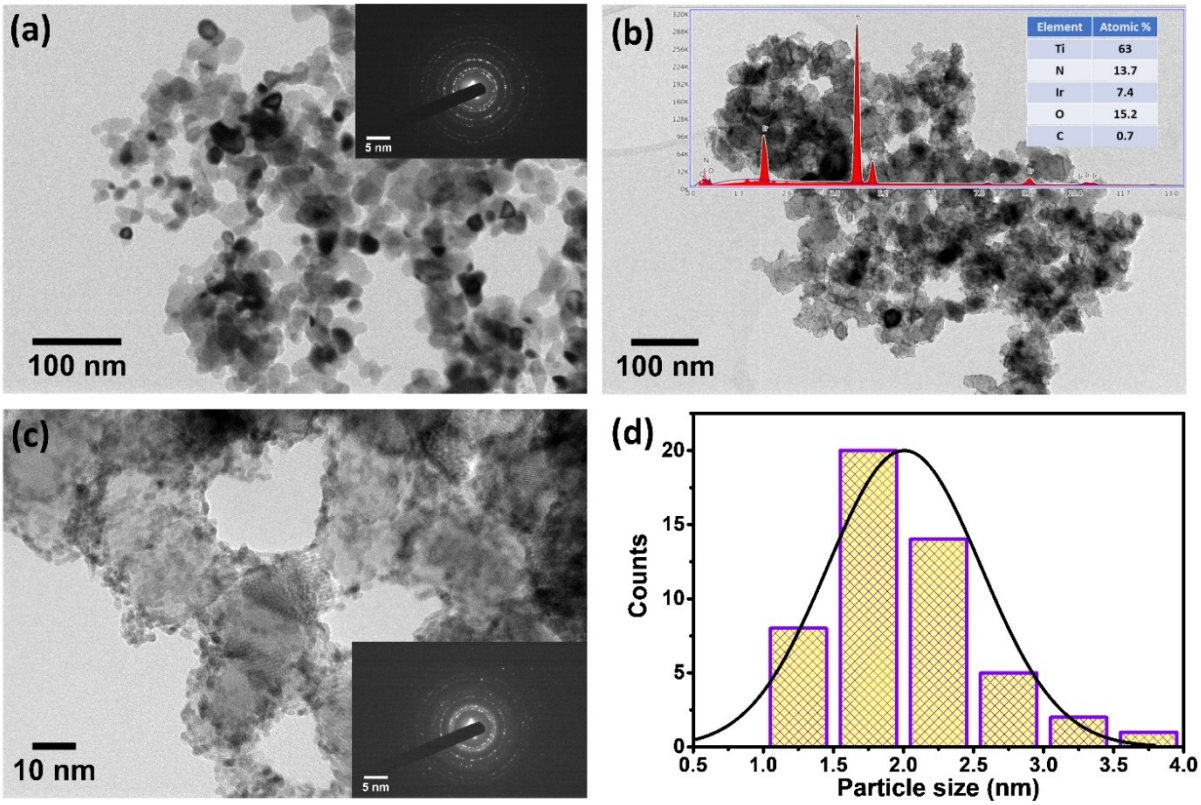

Figure 2. TEM image of (a) bare nano-sized TiN; inset shows SAED pattern, (b) IrO_2@Ir/TiN-40 sample; inset shows the corresponding EDS spectrum and the atomic percent of different elements (c) higher magnification TEM image of IrO_2@Ir/TiN-40 sample; inset shows corresponding SAED pattern; (d) Particle size distribution of the IrO_2@Ir nanoparticles.

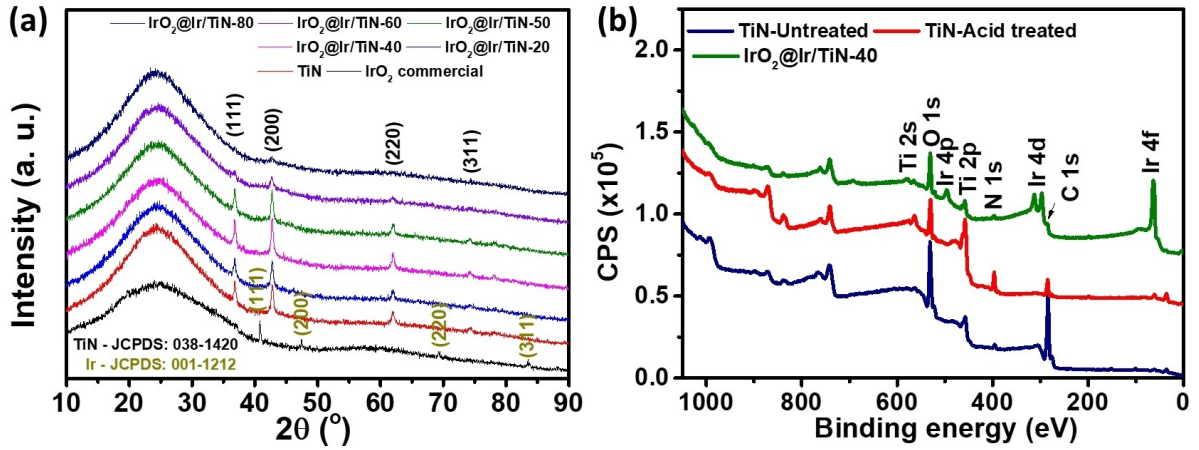

Figure 3. (a) XRD patterns of as synthesized IrO_2@Ir/TiN compositions with bare nano-sized TiN, IrO_2 commercial and (b) XPS survey scan spectrum of as-received TiN, TiN acid-treated and IrO_2@Ir/TiN-40 sample.

corresponding to the TiN support (acid-treated) and the IrO_2@Ir/TiN-40 catalyst was carried out in order to examine the metal support interaction. Pure Ir metal sample (coarse particles) was also analyzed as a reference sample. Table 1 summarizes the binding energies of the deconvoluted peak components for different high resolution XPS peaks of the samples being studied. Figure 4a shows the high resolution Ir 4f XPS spectra for Ir metal and the IrO_2@Ir/TiN-40 samples. The Ir 4f region consists of two distinguishable peaks corresponding to $4f_{7/2}$ and $4f_{5/2}$ spin-orbital splits. Each of the $4f_{7/2}$ and $4f_{5/2}$ components consist of two distinct components corresponding to metallic Ir and Ir^{4+}, where the later corresponds to presence of Ir-oxides.[37,38,41] The binding energies of the spin-orbit split components for metallic Ir are 61.1 and 64.2 eV, while those for

Table 1. Binding energies of different high-resolution peaks of XPS narrow scan spectra.

XPS Peak	Deconvoluted Component	Binding energy [eV]			% Abundance of the component		
		Ir metal	TiN	IrO_2@Ir/TiN	Ir metal	TiN	IrO_2@Ir/TiN
Ir $4f_{7/2}$	Ir–Ir	61.1	–	61.1	73.1	–	53.8
	IrO_2	63.3	–	62.8	26.9	–	46.2
Ir $4f5_{/2}$	Ir–Ir	64.2	–	64.2	73.1	–	53.8
	IrO_2	66.4	–	65.9	26.9	–	46.2
Ti $2p_{3/2}$	Ti–N	–	455.2	455.7	–	43.7	47.7
	TiO_xN_y	–	457.9	457.9	–	56.3	52.3
Ti $2p_{1/2}$	Ti–N	–	460.8	461.3	–	43.7	47.7
	TiO_xN_y	–	463.5	463.5	–	56.3	52.3
N 1s	Ti–N	–	399.0	399.3	–	17.1	24.9
	TiO_xN_y	–	396.5	396.5	–	82.9	75.1
O 1s	Ir–O/TiO_xN_y	–	529.6	530.0	–	62.2	53.6
	Ir–OH/Ti–OH	–	531.4	531.5	–	24.5	35.0
	H–O–H	–	533.1	533.2	–	13.3	11.4

the Ir^{4+} are 63.3 and 66.4 eV. For the IrO_2@Ir/TiN-40 sample, while the metallic Ir components have the binding energy values identical to the corresponding values for the Ir metal sample, the Ir^{4+} components show a shift of 0.5 eV towards lower binding energy, suggesting (i) an interaction between the IrO_2 and TiN support, with shifting of the electron cloud from Ti to IrO_2@Ir and/or (ii) the Ir oxidation state of the Ir-oxide phase in the synthesized sample being the Ir^{x+}, with $x<4$. The fractional area corresponding to Ir^{4+} in the Ir 4f region is 27% for Ir metal and 46% for IrO_2@Ir/TiN-40 sample (Table 1). The Ir^{4+} contribution higher than that from the native surface oxide indicates presence of both the metallic Ir and IrO_2 in the synthesized sample. This, combined with the observed XRD patterns, suggesting formation of amorphous phase, suggests the Ir-based nanoparticles consisting of an IrO_2 core with a metallic Ir surface, possibly an imperfect shell, which shows no diffraction peaks due to its low thickness (a few atomic layers thick).

Formation of such a structure may be explained by looking into the synthesis reaction. Here, the observed amorphous structure may be attributed to the poor reducibility of EG for the Ir^{3+} ions at the reaction temperature of 140 °C. For example, Luo et al.[42] have stated that EG requires a relatively high temperature (>170 °C) to upsurge reduction rate whereas it drastically diminishes when the temperature is decreased. Hence, the formation of amorphous phase possibly takes place through hydrolysis of intermediate Ir-hydroxide species (leading to formation of amorphous Ir-Oxide) followed by reduction of the surface to metallic Ir. Such a formation of lower oxidation state Ir species (e.g. Ir^{+}) under microwave-assisted heating to higher temperatures (>140 °C) in presence of ethylene glycol has also been reported previously.[43]

Further, the high-resolution Ti 2p XPS spectra of TiN with/without Ir loading (Figure 4b) could be deconvoluted into a pair of two the spin-orbital components corresponding to Ti $2p_{3/2}$ and Ti $2p_{1/2}$. Each of the spin-orbital component consists of two sub-components ascribed to the Ti–N and TiO_xN_y at the respective binding energies of ~455.7 and ~457.9 eV for the Ti $2p_{3/2}$ component, where for the latter, both N and O are bound to Ti (O–Ti–N), instead of a Ti–N–O or Ti–O–N bonds.[38,44–47] The binding energies of different components and their relative abundances are listed in Table 2. Notably, a shift of 0.5 eV towards higher binding energy in the peak position of Ti–N bond is observed for the TiN coated with the IrO_2@Ir nanoparticles, which indicates a IrO_2@Ir-TiN interaction. The shift in binding energy can be attributed to the lower electronegativity of Ti (1.54) as compared to that of Ir (2.20), leading to a shifting of the electron cloud towards IrO_2@Ir species from the Ti and hence a shift towards higher binding energy for Ti with a corresponding shift towards lower energy for IrO_2.

Further, Figure 4c exhibits the high-resolution N 1s spectra of the acid-treated TiN and the IrO_2@Ir/TiN-40 samples. Each N 1s spectrum was deconvoluted into two peaks at ~396.5 and ~399.0 eV, which correspond respectively to TiO_xN_y and Ti–N,[45–48] owing to the presence of O–Ti–N bonds on the TiN surface.[49,50] For the IrO_2@Ir/TiN-40 sample, the Ti–N component of the N 1s spectrum shows a shift of 0.3 eV towards higher binding energy w.r.t. that of bare support. This could be explained through shifting of the electron cloud away from N due to Ti–Ir interaction.

The relative area fractions (abundances) of the Ti–N and TiO_xN_y components for bare TiN are ~44% and 56% when viewed from Ti 2p peak, while the N 1s peak exhibits their respective abundances of ~17% and 83%. The discrepancy may be due to presence of the TiO_xN_y phase on the surface of the bulk TiN particle and hence lower XPS signal of N 1s from bulk TiN compared to the Ti 2p signal as the surface TiO_xN_y layer reduces the N 1s signal more efficiently compared to the Ti 2p signal. Furthermore, for both the N 1s and Ti 2p peaks, abundance of Ti–N remains higher for IrO_2@Ir/TiN as compared to that for bare TiN (Table 1), probably partial reduction of the surface TiO_xN_y during the MW synthesis.

Table 2. Impact of AST on catalyst performance.

Sample	Mass activity [A g^{-1}]		Retention [%]	Ir mass loss [μg]	Ir mass loss [%]
	Initial	Final			
IrO_2@Ir/TiN-UT-40	715	388	54	0.88	11
IrO_2@Ir/TiN-40	663	525	79	0.51	7
IrO_2 comm.	281	186	66	0.51	3

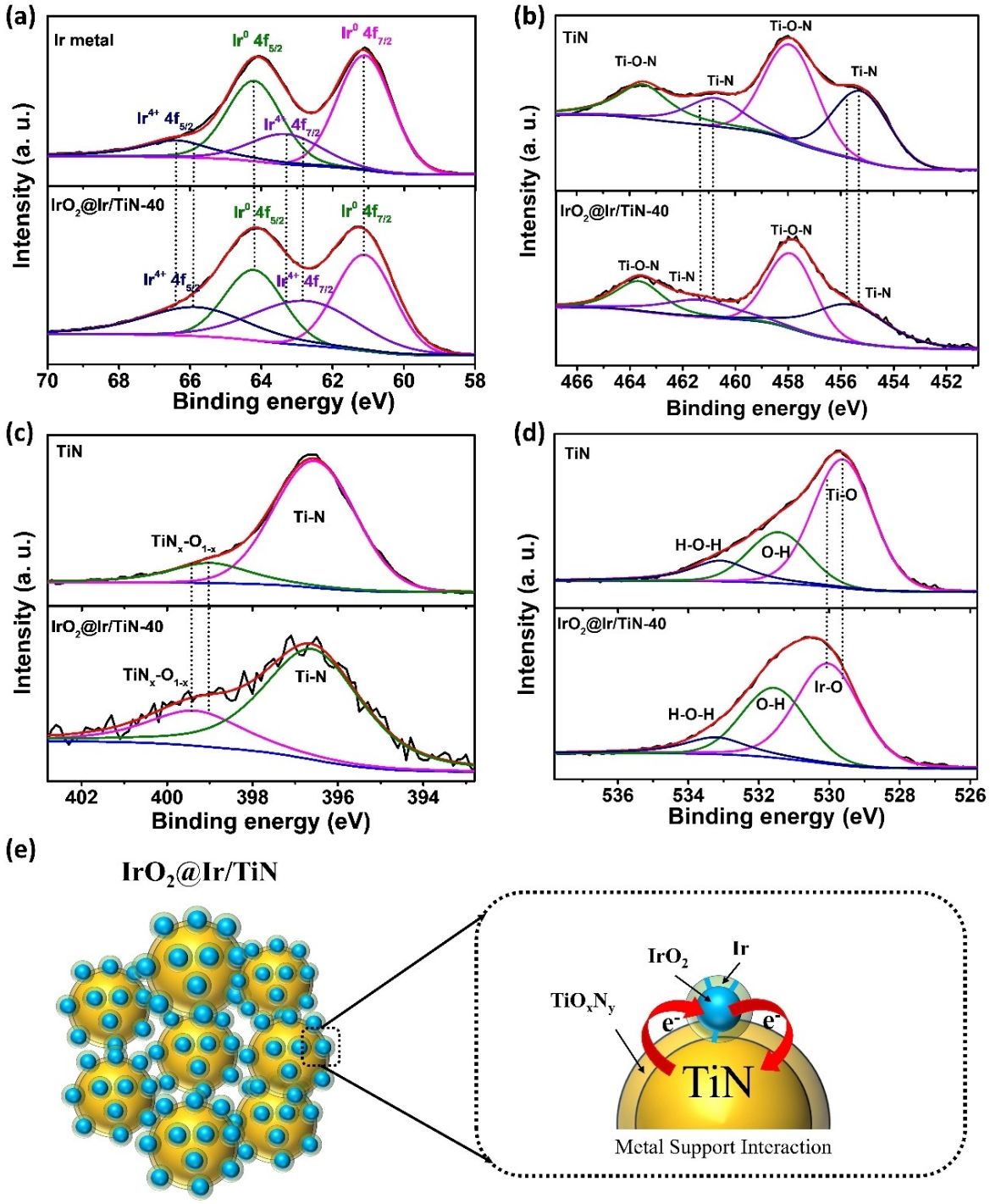

Figure 4. (a) High resolution XPS spectra corresponding to (b) Ir 4f peak for Ir metal and IrO_2@Ir/TiN samples, and (b) Ti 2p, (c) N 1s, and (d) O 1s peaks for acid-treated nano TiN and IrO_2@Ir/TiN-40 samples. (e) Schematic presentation of metal support interaction between IrO_2@Ir and TiN.

Figure 4d shows a comparison of the O 1s spectra of TiN and IrO_2@Ir/TiN-40, which were deconvoluted into three peaks: the lattice oxygen (TiO_xN_y and Ir–O at 529.6 eV for the bare TiN support and at 530.0 eV for IrO_2@Ir/TiN-40), the oxygen in hydroxyl group (O–H) at ~531.5 eV and the oxygen in adsorbed water (H–O–H) at ~533.2 eV. From Table 1, it is clear that the O–H peak abundance increases significantly after the coating of IrO_2@Ir nanoparticles on the surface of TiN. This indicates existence of O–H bound to Ir species after the coating of IrO_2@Ir nanoparticles. Hydrated or hydroxylated amorphous iridium oxides are generally more active toward OER than the excellent crystalline IrO_2.[51,52] Finally, the metal support interaction is presented schematically in Figure 4e, illustrating electron cloud shifting from Ti to Ir.

Surface area and porosity study: Excellent porous structure and high surface area are the significant aspects that should be considered for choosing a proper support material. They are also favorable factors for improving the performance of supported catalysts because they provide a highly dispersed physical surface for the active component on which catalytic reactions take place. Figure 5a illustrates N_2 adsorption/desorption isotherm curves for as-received and acid-treated TiN samples. For both samples, the isotherms exhibit hysteresis loop for the relative pressure (p/p°) >0.85, indicating the presence of mesoporous structures. There is no significant change found in the surface area after acid treatment (as-received TiN: 60.8 $m^2 g^{-1}$; acid-treated TiN: 58.6 $m^2 g^{-1}$), calculated using the data between 0 to 0.35 (P/P_0). However, the acid-treated sample exhibits larger adsorption for $P/P_0 > 0.85$, probably indicating the increased accessibility of the mesopores, through pore opening or surface energy change (change of wettability characteristics) due to acid-treatment. According to the pore size distribution obtained by applying the BJH model for the adsorption branches of isotherms (Figure 5b), the pore diameters of as-received and acid-treated TiN samples are centered at ~3 nm, confirming their mesoporous structure.

Durability study through AST: To study the electrochemical stability of the synthesized electrocatalysts through AST, the sample showing the best initial OER activity, i.e., IrO_2@Ir/TiN-40 was selected. Another IrO_2@Ir/TiN catalyst sample, with 40 wt% Ir loading on the as-received TiN support (IrO_2@Ir/TiN-UT-40), synthesized under the synthesis conditions identical to those used for IrO_2@Ir/TiN-40, was also studied to investigate the effect of surface chemical state on degradation. Moreover, AST of the commercial IrO_2 is included for comparison. Figures 6a–c show the initial and final OER polarization curves of the IrO_2@Ir/TiN-UT-40, IrO_2@Ir/TiN-40 and commercial IrO_2 catalysts, respectively. The corresponding OER activity degradation patterns (in terms of retention %) are shown as insets in Figures 6a–c. The IrO_2@Ir/TiN-UT-40 sample (supported on as-received TiN), having an initial mass activity of 715 A/g (Table 2), shows a 54% retention of the OER activity after 2000 cycles with a 43 mV increase in the overpotential. On the other hand, the IrO_2@Ir/TiN-40 catalyst (supported on acid-treated TiN), having an initial mass activity of 663 A/g, shows an OER activity retention of 79% by sacrificing only 22 mV of the overpotential. Hence, the acid treatment process clearly improves the catalyst durability, possibly through the modified surface characteristics of the TiN support during the acid-treatment. Furthermore, the IrO_2@Ir/TiN-40 catalyst shows a superior durability compared to that of the commercial IrO_2 catalyst with a retention of 66% by sacrificing 25 mV of the overpotential, which makes it a promising OER catalyst.

Comparison of the XRD patterns before and after AST of the studied electrocatalysts has been shown in Figures 6d–f for the IrO_2@Ir/TiN-UT, IrO_2@Ir/TiN-40 and commercial IrO_2 catalysts, respectively. No obvious change has been observed in the XRD patterns recorded before and after AST, suggesting no significant changes in the bulk structure of the support or IrO_2@Ir during AST. Moreover, the Ir mass loss due to catalyst and support material dissolution and/or detachment from the electrode, evaluated by measuring the Ir content on the electrode before and after AST, show relatively similar values (Table 2), with the catalyst supported on the acid-treated TiN showing marginally lower Ir loss. This could be attributed to the presence of surface functional groups on the acid-treated support that could act as the redeposition centers for the dissolved Ir and hence lead to reduced Ir loss. For both of the supported catalysts, no Ti loss were observed from the XRF analysis of the electrodes before and after AST. XRF spectra of the IrO_2@ Ir/TiN-40 and @IrO_2@ Ir/TiN -UT samples, recorded before and after AST, are shown in Figures 7a and b, respectively. It reveals the X-ray emission lines of Ti $K_{\alpha 1}$, Ir $L_{\alpha 1}$, and Ir $L_{\beta 1}$ at corresponding energy values of 5.51, 9.18, and 10.71 keV over the GC RDE background. Peak intensities of the Ti K_α Ir $L_{\alpha 1}$, and Ir $L_{\beta 1}$ spectral lines show no difference in peak area for the spectra recorded before and after the AST. This indicates the nano-sized TiN as a promising robust support for IrO_2@Ir nanodots.

Degradation mechanisms: Mechanistic insights into the OER activity degradation during AST are revealed through post-AST analysis of the electrocatalysts. Here, we attribute the loss of

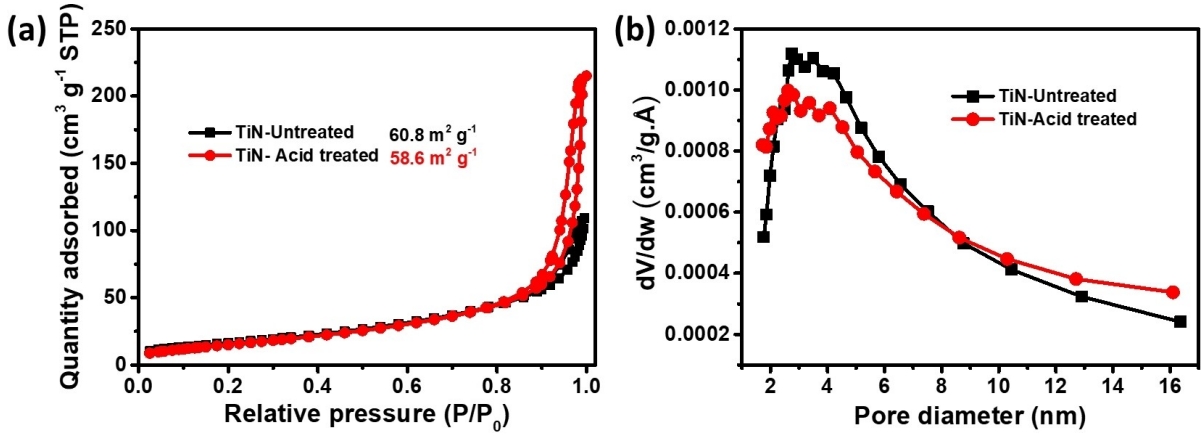

Figure 5. (a) N_2 adsorption/desorption isotherm (b) Pore size distribution for TiN samples before and after acid treatment.

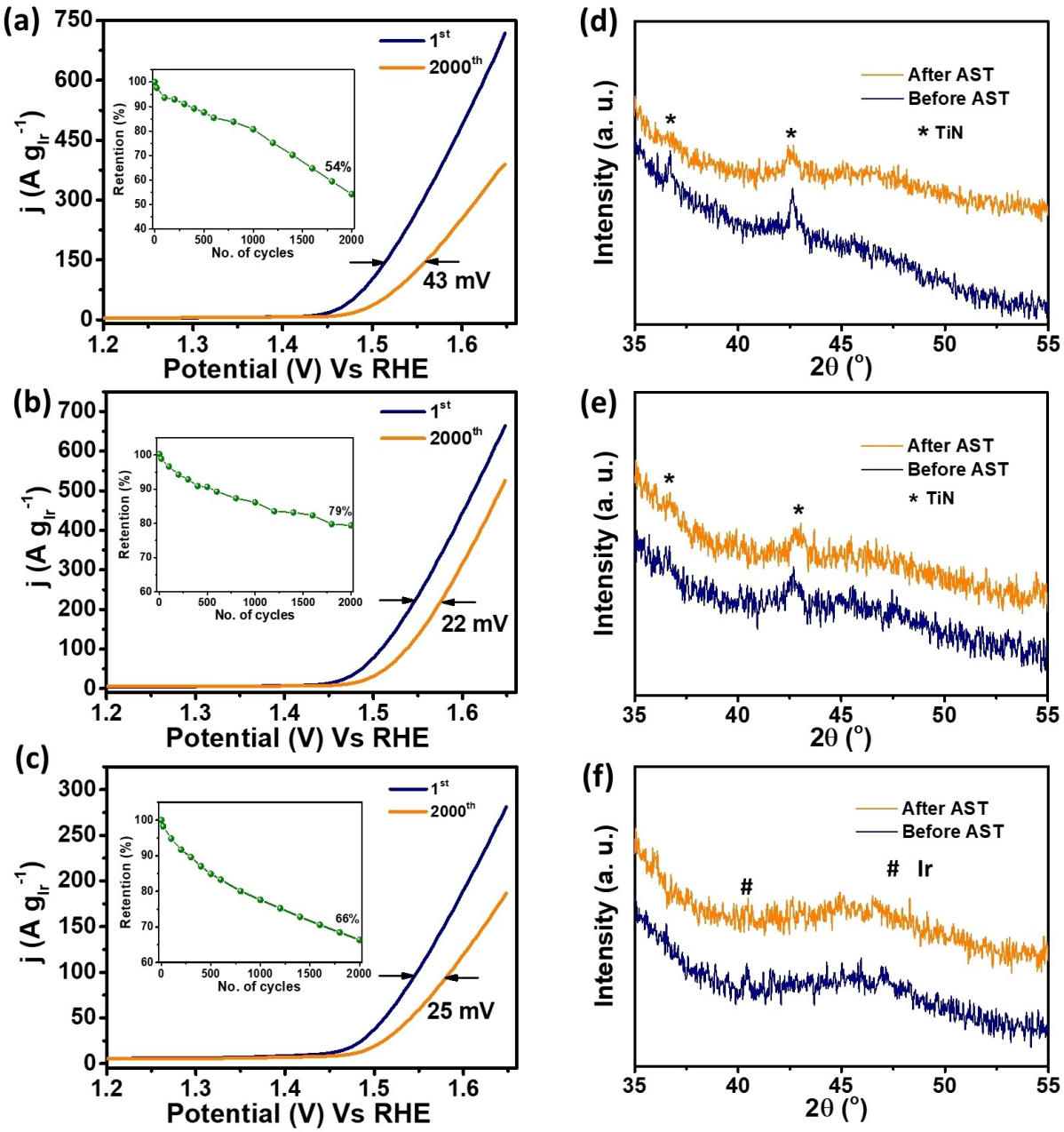

Figure 6. OER polarization curves recorded before the 1st and after the 2000th stress cycle during AST of (a) IrO_2@Ir/TiN-UT, (b) IrO_2@Ir/TiN-40, and (c) IrO_2 commercial catalysts. Insets in (a), (b) and (c) show the corresponding variations of the OER activity with the number of stress cycles. XRD patterns of (d) IrO_2@Ir/TiN-UT, (e) IrO_2@Ir/TiN-40 and (f) IrO_2 commercial catalysts before and after the AST.

OER activity during AST solely to the loss of catalyst surface available for the electrocatalytic reaction, which comprises different mechanisms such as (i) particle growth during AST or agglomeration of individual catalyst particles, (ii) loss of the catalyst from the electrode surface through dissolution and detachment, (iii) corrosion of the catalyst support etc.

As can be seen from Table 2, the degradation of OER activity during AST cannot be attributed completely to the loss of catalyst through dissolution/detachment. Hence, further investigation of the post-AST IrO_2@Ir/TiN-40 sample through TEM was performed. As shown in Figure 8, the post-AST electrocatalyst shows a microstructure like that of the as-synthesized sample (shown in Figure 2). The catalyst nanodots remain supported on the TiN support and the state of agglomeration remains unaffected during AST. The average particle size of the electrocatalyst increases from 2.0 nm (as synthesized) to 2.4 nm (post-AST), leading to reduction in the available surface area and hence to a reduced OER activity. Further, as the post-AST Ir loading determination through XRF shows ~7% loss, which is comparable to that for the unsupported commercial sample (~3% loss). Because the dissolution of Ir through electrochemical treatments during AST may depend significantly on the surface

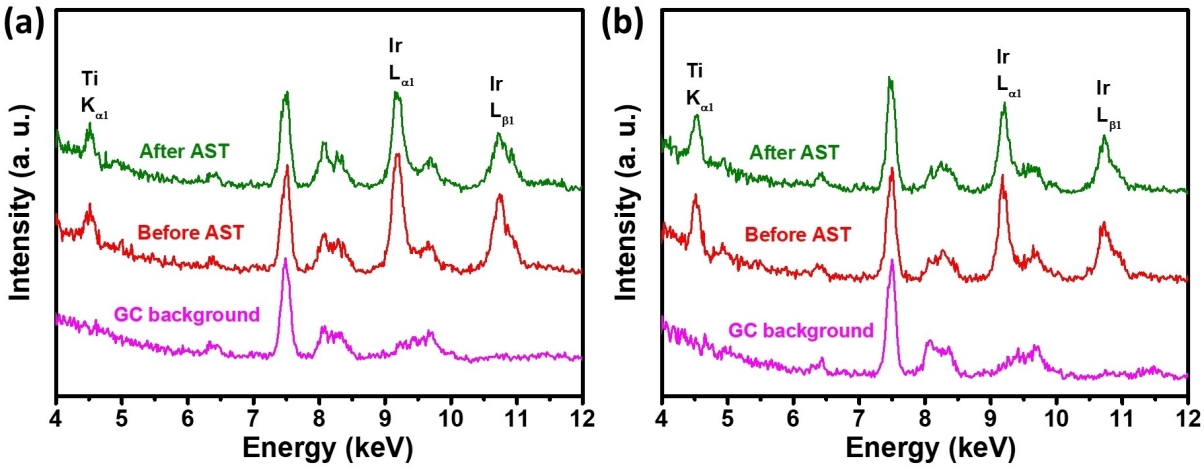

Figure 7. XRF spectra of (a) IrO_2@Ir/TiN-40 and (b) IrO_2@Ir/TiN -UT catalysts coated on GC RDE, recorded before and after AST.

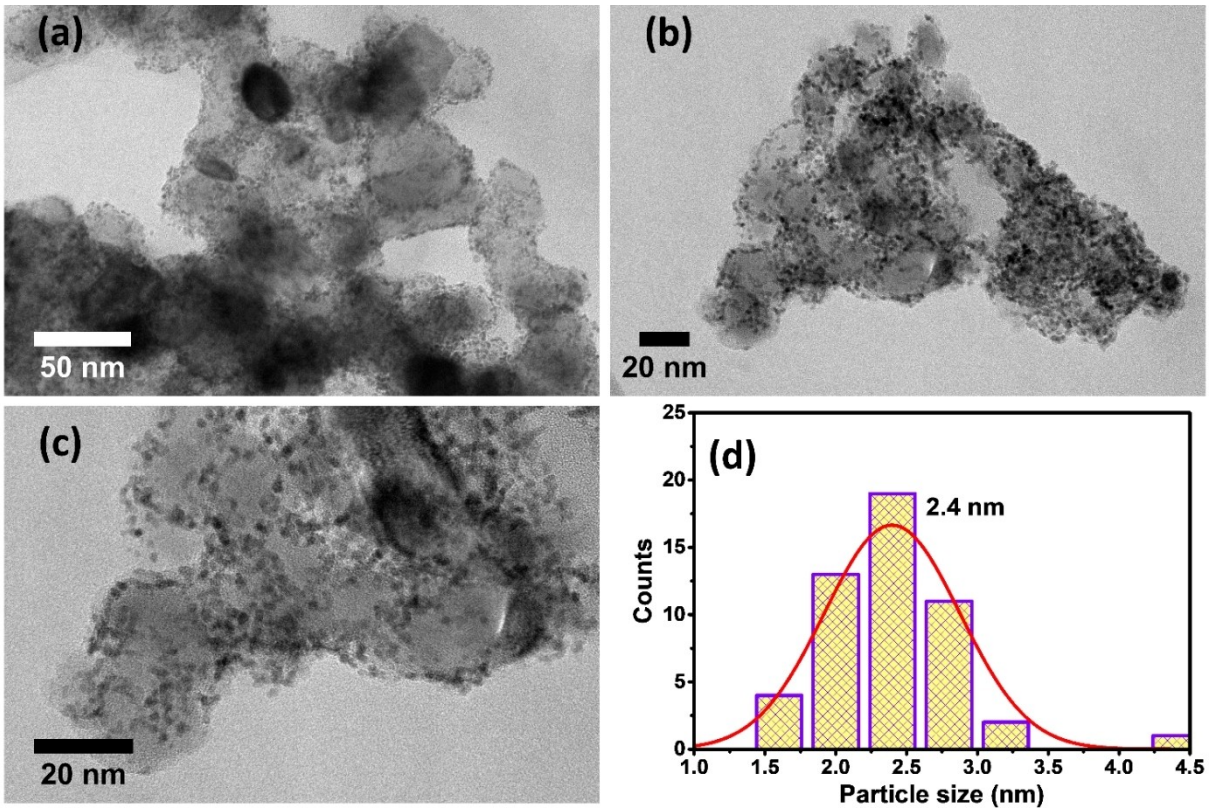

Figure 8. (a–c) TEM images and (d) particle size distribution of the post-AST IrO_2@Ir/TiN-40 sample

chemistry of the catalyst nanoparticles, the observed 7% loss of Ir loading can be assigned to dissolution. Lastly, no observable detachment of the catalyst from the support suggests the activity loss due to support corrosion to be negligible. This is also supported by the facts that (i) the XRD analysis of the catalysts before and after AST reveal no significant degradation of TiN for both the IrO_2@Ir/TiN-UT and the IrO_2@Ir/TiN-40 samples (Figures 6d&e) and (ii) the XRF spectra of the electrodes, recorded before and after AST, show no sign of Ti dissolution from the electrode (Figure 7a&b).

Future prospects: Ir-based catalysts are well known for their high OER activity. However, reduction of the required catalyst loading along with maintaining or enhancing the performance of the catalyst is a challenging task. As TiN has shown its potential as an efficient, stable and corrosion-free support for Ir-based nanoparticles, it opens up new possibilities for nano-sized TiN support. Although the presented results are limited to

the upper potential of 1.7 V, considering the effectiveness of the synthesis process, the highly conductive and corrosion resistant TiN can be used further as a support material for other precious or non-precious metal nanoparticles to be used in electrochemical energy conversion and storage devices. Furthermore, the study focuses on the catalyst support interaction through studying the surface chemical states of the synthesized catalysts. Theoretical understanding of the correlations between the intrinsic activity and the catalyst/support interaction through *ab-initio* calculations may be explored further.

Conclusions

In conclusion, we have produced a series of TiN-supported IrO_2@Ir electrocatalyst for OER in an acidic environment using a facile microwave assisted polyol synthesis. The optimized composition IrO_2@Ir/TiN-40 sample (40 wt% Ir on TiN) featured a decoration of IrO_2@Ir nanodots on the surface of TiN nanoparticles. The nano TiN support provided a high surface area ($58\ m^2\ g^{-1}$) and strong interaction with the catalyst, leading to uniform dispersion of the fine IrO_2@Ir nanoparticles with 2 nm diameter. The IrO_2@Ir/TiN-40 catalyst demonstrates an outstanding mass normalized OER activity of 637 A g_{Ir}^{-1} at 1.65 V, which is 2.4 times that of the commercial IrO_2 catalyst. Further, a potentiodynamic durability study also suggested high stability of the synthesized electrocatalyst with a retention rate of 79%, which is also an advantage over the unsupported IrO_2 catalyst. Quantification of the degradation mechanisms of the supported catalyst revealed no measurable support corrosion, while 30% and 70% of the observed activity loss are attributed to Ir catalyst dissolution and particle size growth, respectively. This strongly suggests that the present strategy based on the nano-sized TiN support is highly promising and have the potential to reduce Ir loading in PEM electrolyzers by 80% without compromising either activity or lifetime. Such a reliable and highly efficient supported OER catalyst could contribute to a market expansion of PEM electrolysis technology and accelerate the global green hydrogen production.

Experimental Section

Chemicals: The metal precursor iridium(III) chloride hydrate ($IrCl_3.xH_2O$; Sigma-Aldrich), the solvent ultrapure water having a resistivity $>18.2\ M\Omega$ cm (milliQ), the reducing agent ethylene glycol (EG; anhydrous, 99.8%, Sigma-Aldrich), perchloric acid ($HClO_4$, 98%, Sigma-Aldrich) and hydrochloric acid (HCl, 37%; Sigma-Aldrich) for preparing the electrolyte/reaction bath were used without further treatments. Titanium nitride (99.99% TiN, Alroko®) having an average particle size of 20 nm, was used as the catalyst support as-received as well as after an acid treatment.

Acid treatment of TiN: Acid treatment of the TiN powder was carried out in order to clean and activate the surface. The TiN powder (500 mg) was mixed with 25 mL of conc. HCl (37 wt%) and held at 65 °C for 1 h. Further, the acid-treated TiN sample centrifuged and washed several times with ultrapure water until neutral pH, before drying in a vacuum oven overnight at 60 °C.

Preparation of TiN supported IrO_2@Ir nanoparticles: The IrO_2@Ir/TiN electrocatalysts were synthesized by utilizing a microwave-assisted modified polyol synthesis method using a CEM Discovery SP® microwave synthesizer. The equipment was operated in a dynamic power mode with a maximum power output of 200 W. The reaction parameters for the IrO_2@Ir/TiN samples produced in this work are summarized in Table 3. In a typical synthesis, the required amount of the $IrCl_3 \cdot H_2O$ solution in ultrapure water (Ir conc. 5 mM) was mixed with EG to obtain an EG/water ratio of 3:7 (v/v). Further, the required amount of acid-treated TiN (TiN-AT) powder (based on the desired Ir wt%) was dispersed in the mixture through ultrasonication for 60 s at room temperature using a Hielscher UP200 St ultrasonic homogenizer. The mixture (~20 mL), kept in a 35 mL glass reactor, was exposed to a microwave treatment for 20 min at a reaction temperature of 140 °C under closed system conditions. After cooling, the sample was collected by centrifugation at 5000 rpm for 5 min, followed by washing the precipitate thrice with ultrapure water and drying overnight at 60 °C. Figure 9 illustrates the schematic presentation of IrO_2@Ir/TiN synthesis process. For comparison, an IrO_2@Ir/TiN sample with an Ir loading of 40 wt% was also synthesized using the as-received/untreated TiN (TiN-UT).

Electrochemical characterizations: Electrochemical characterizations were performed using a three-electrode setup with the catalyst coated GC RDE acting as the working electrode (WE) and a Pt wire acting as the counter electrode. The potentials were measured w.r.t. an Ag/AgCl reference electrode (Aldrich; double junction; sat. KCl) and reported w.r.t. the reversible hydrogen electrode (RHE). The electrochemical experiments were carried out using a Zahner-IM6e electrochemical workstation. In a typical process, 10 mg of the IrO_2@Ir/TiN catalyst was dispersed by ultrasonication for 60 s in 5 mL of a stock solution containing 1.84 v% of 5 wt% Nafion, 20 v% of isopropyl alcohol, and 78.16 v% of ultrapure water.

Table 3. Experimental parameters used for the synthesis of different IrO_2@Ir/TiN compositions.

Sample ID	Support	Support [wt%]	Ir [wt%]	Solvent [mL]	$IrCl_3$ [mM]
IrO_2@Ir/TiN-20	TiN (acid-treated)	80	20	6 + 14 (3/7 : EG/Water)	5
IrO_2@Ir/TiN-40	TiN (acid-treated)	60	40	6 + 14 (3/7 : EG/Water)	5
IrO_2@Ir/TiN-50	TiN (acid-treated)	50	50	6 + 14 (3/7 : EG/Water)	5
IrO_2@Ir/TiN-60	TiN (acid-treated)	40	60	6 + 14 (3/7 : EG/Water)	5
IrO_2@Ir/TiN-80	TiN (acid-treated)	20	80	6 + 14 (3/7 : EG/Water)	5
IrO_2@Ir/TiN-UT	TiN (as-received)	60	40	6 + 14 (3/7 : EG/Water)	5

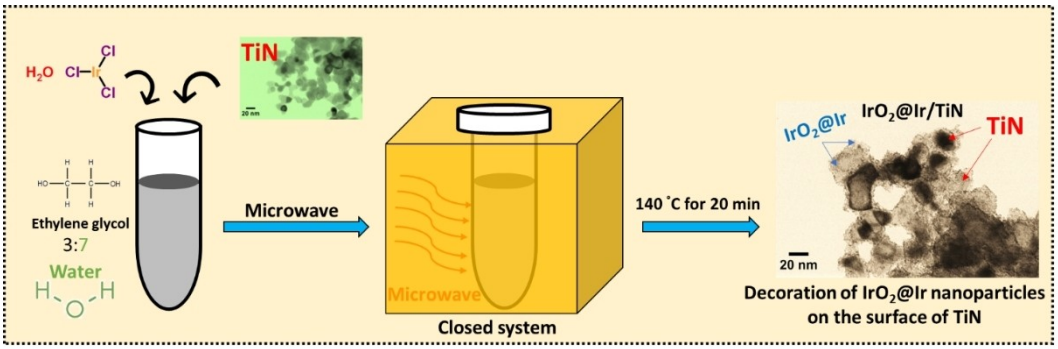

Figure 9. Schematic presentation of IrO_2@Ir/TiN synthesis process.

Further, to prepare the WE, 10 μL of the dispersed catalyst was loaded on a glassy carbon rotating disc electrode (GC RDE; diameter: 5 mm) and dried under rotator at 700 rpm. The Ir loading on the GC RDE was measured using XRF analyzer (Thermo Scientific Niton XL3t GOLDD+), as described in our earlier study.[53]

The oxygen evolution reaction (OER) activity of the catalyst was measured in accordance with the methodology given by Alia,[39] with minor changes. In summary, the electrode was activated in nitrogen-saturated 0.1 M $HClO_4$ by potential cycling for 20 cycles between 1.00 and 1.70 V at a scan rate of 100 mV s^{-1} and a rotation speed of 1600 rpm prior to OER measurements. Potential cycling in the same electrolyte for two cycles between 1.00 and 1.65 V at a scan rate of 10 mV s^{-1} and a rotation speed of 1600 rpm, termed as observational cycling, was performed and the positive-going segment of the second cycle was used for the OER activity determination. Mass specific OER of the catalysts is reported as the observed current at 1.65 V per unit mass of Ir metal, during the positive-going scan of the observational cycling. Further, to assess the durability of the catalyst, AST was performed in a nitrogen-saturated 0.1 M $HClO_4$ solution at room temperature through cyclic voltammetry in the range of 1.00–1.70 V for 2000 cycles at a scan rate of 100 mV s^{-1} (stress cycling) along with intermediate observational cycling after specified number of stress cycles. Loss of Ir during AST was estimated using the Ir loadings (XRF measurement) before and after AST.

Structural characterizations: A Rigaku Miniflex 600 X-ray diffractometer equipped with Cu Ka radiation ($\lambda = 1.5418$ Å) was used to obtain the X-ray diffraction (XRD) patterns of the IrO_2@Ir/TiN samples, where a scan rate of 3°/min and a step size of 0.02° was used. X-ray photoelectron spectroscopy (XPS) was used to investigate the surface chemistry of the IrO_2@Ir/TiN samples using a SPECS® XPS system with a twin anode X-ray source and a hemispherical analyzer and $Mg_{K\alpha}$ (1253.6 eV) radiation. Ir metal powder was used to compare the wide scan spectra corresponding to Ir 4f peak. The elemental makeup of solid surfaces is examined using energy-dispersive X-ray spectroscopy (EDS; Oxford, x-max). The transmission electron microscope (TEM) images were recorded using JEOL JEM-2010F TEM in order to investigate morphology and particle size of the synthesized IrO_2@Ir/TiN samples. The particle size distributions of Ir nanoparticles were determined by analyzing the TEM images with ImageJ software. The dark contract of Ir nanoparticles distinguished them from the TiN support background. For a typical sample, 50 nanoparticles from various images were individually analyzed. Surface areas and pore size distributions of the synthesized catalysts were evaluated via N_2 adsorption/desorption measurements (Micromeritics Tristar II Plus Surface Area & Porosity Analyser).

Acknowledgements

The authors acknowledge Rikke Klindt Müller, IGT SDU for performing the surface area and porosity measurements. The authors also acknowledge the financial support from Danish Energy Agency EUDP project 3R, Nr. 64019-0551; Innovation Fund Denmark, InnoExplorer program, Nr. 9122-00112; Danish ESS lighthouse on hard materials in 3D, SOLID, Grant number 8144-00002B and the Energi Fyn development fund and Slovenian Research Agency (research core funding Nos. P2-0089). We acknowledge the CENN Nanocenter for the use of the Transmission Electron Microscope Jeol JEM-2100.

Conflict of Interest

The authors declare no conflict of interest.

Data Availability Statement

The data that support the findings of this study are available on request from the corresponding author. The data are not publicly available due to privacy or ethical restrictions.

Keywords: iridium oxide@iridium · microwave · oxygen evolution reaction · titanium nitride · titanium oxonitride

[1] J. Suntivich, K. J. May, H. A. Gasteiger, J. B. Goodenough, Y. Shao-Horn, *Science* **2011**, *334*, 1383–1385.
[2] H. Dau, C. Limberg, T. Reier, M. Risch, S. Roggan, P. Strasser, *ChemCatChem* **2010**, *2*, 724–761.
[3] M. E. G. Lyons, S. Floquet, *Phys. Chem. Chem. Phys.* **2011**, *13*, 5314–5335.
[4] M. Carmo, D. L. Fritz, J. Mergel, D. A. Stolten, *Int. J. Hydrogen Energy* **2013**, *38*, 4901–4934.
[5] J. Yu, Y. Guo, S. She, S. Miao, M. Ni, W. Zhou, M. Liu, Z. Shao, *Adv. Mater.* **2018**, *30*, 1800047.
[6] J. Yu, X. Wu, Y. Zhong, G. Yang, M. Ni, W. Zhou, Z. Shao, *Chem. Eur. J.* **2018**, *24*, 13800–13806.
[7] G. Li, S. Li, M. Xiao, J. Ge, C. Liu, W. Xing, *Nanoscale* **2017**, *9*, 9291–9298.
[8] E. Antolini, *ACS Catal.* **2014**, *4*, 1426–1440.
[9] X. Li, X. Hao, A. Abudula, G. Guan, *J. Mater. Chem. A* **2016**, *4*, 11973–12000.

[10] J. Feng, F. Lv, W. Zhang, P. Li, K. Wang, C. Yang, B. Wang, Y. Yang, J. Zhou, F. Lin, G.-C. Wang, S. Guo, *Adv. Mater.* **2017**, *29*, 1703798.
[11] I. C. Man, H.-Y. Su, F. Calle-Vallejo, H. A. Hansen, J. I. Martínez, N. G. Inoglu, J. Kitchin, T. F. Jaramillo, J. K. Nørskov, J. Rossmeisl, *ChemCatChem* **2011**, *3*, 1159–1165.
[12] H.-S. Oh, H. N. Nong, T. Reier, A. Bergmann, M. Gliech, J. Ferreira de Araújo, E. Willinger, R. Schlögl, D. Teschner, P. Strasser, *J. Am. Chem. Soc.* **2016**, *138*, 12552–12563.
[13] T. Reier, Z. Pawolek, S. Cherevko, M. Bruns, T. Jones, D. Teschner, S. Selve, A. Bergmann, H. N. Nong, R. Schlögl, K. J. J. Mayrhofer, P. Strasser, *J. Am. Chem. Soc.* **2015**, *137*, 13031–13040.
[14] L. Ma, S. Sui, Y. Zhai, *J. Power Sources* **2008**, *177*, 470–477.
[15] S. Sharma, B. G. Pollet, *J. Power Sources* **2012**, *208*, 96–119.
[16] P. Mazúr, J. Polonský, M. Paidar, K. Bouzek, *Int. J. Hydrogen Energy* **2012**, *37*, 12081–12088.
[17] C. Spüri, J. T. Kwan, A. Bonakdarpour, D. P. Wilkinson, P. Strasser, *Angew. Chem. Int. Ed.* **2017**, *56*, 5994–6021; *Angew. Chem.* **2017**, *129*, 6088–6117.
[18] J. Wang, G. Yin, Y. Shao, S. Zhang, Z. Wang, Y. Gao, *J. Power Sources* **2007**, *171*, 331–339.
[19] E. Antolini, E. R. Gonzalez, *Appl. Catal. B* **2009**, *365*, 1–19.
[20] L. Wang, P. Lettenmeier, U. Golla-Schindler, P. Gazdzicki, N. A. Cañas, T. Morawietz, R. Hiesgen, S. S. Hosseiny, A. S. Gago, K. A. Friedrich, *Phys. Chem. Chem. Phys.* **2016**, *18*, 4487–4495.
[21] W. Hu, S. Chen, Q. Xia, *Int. J. Hydrogen Energy* **2014**, *39*, 6967–6976.
[22] H.-S. Oh, H. N. Nong, T. Reier, M. Gliech, P. Strasser, *Chem. Sci.* **2015**, *6*, 3321–3328.
[23] G. Liu, J. Xu, Y. Wang, X. Wang, *J. Mater. Chem. A* **2015**, *3*, 20791–20800.
[24] F. Karimi, B. A. Peppley, *Electrochim. Acta* **2017**, *246*, 654–670.
[25] R. E. Fuentes, H. R. Colón-Mercado, M. J. Martínez-Rodríguez, *J. Electrochem. Soc.* **2013**, *161*, F77–F82.
[26] J. Polonský, P. Mazúr, M. Paidar, E. Christensen, K. Bouzek, *Int. J. Hydrogen Energy* **2014**, *39*, 3072–3078.
[27] J. Polonský, I. M. Petrushina, E. Christensen, K. Bouzek, C. B. Prag, J. E. T. Andersen, N. J. Bjerrum, *Int. J. Hydrogen Energy* **2012**, *37*, 2173–2181.
[28] J. Polonský, P. Mazúr, M. Paidar, K. Bouzek, *J. Solid State Electrochem.* **2014**, *18*, 2325–2332.
[29] A. V. Nikiforov, A. L. Tomás García, I. M. Petrushina, E. Christensen, N. J. Bjerrum, *Int. J. Hydrogen Energy* **2011**, *36*, 5797–5805.
[30] M. Yang, Z. Cui, F. J. DiSalvo, *Phys. Chem. Chem. Phys.* **2013**, *15*, 1088–1092.
[31] M. M. Ottakam Thotiyl, T. Ravikumar, S. Sampath, *J. Mater. Chem.* **2010**, *20*, 10643–10651.
[32] O. T. M. Musthafa, S. Sampath, *Chem. Commun.* **2008**, *1*, 67–69.
[33] S. Yang, J. Kim, Y. J. Tak, A. Soon, H. Lee, *Angew. Chem. Int. Ed.* **2016**, *55*, 2058–2062; *Angew. Chem.* **2016**, *128*, 2098–2102.
[34] Y. Zheng, J. Zhang, H. Zhan, D. Sun, D. Dang, X. L. Tian, *Electrochem. Commun.* **2018**, *91*, 31–35.
[35] S. Yang, J. Kim, Y. J. Tak, A. Soon, H. Lee, *Angew. Chem. Int. Ed.* **2016**, *55*, 2058–2062; *Angew. Chem.* **2016**, *128*, 2098–2102.
[36] Y. Zheng, J. Zhang, H. Zhan, D. Sun, D. Dang, X. L. Tian, *Electrochem. Commun.* **2018**, *91*, 31–35.
[37] G. Li, L. Li, L. Yang, J. Chang, R. Ma, Z. Wu, W. Xing, *ACS Appl. Mater. Interfaces* **2018**, *10*, 38117–38124.
[38] K. Zhang, W. Mai, J. Li, G. Liand, G. Li, W. Hu, *J. Mater. Sci.* **2020**, *55*, 3507.
[39] S. M. Alia, G. C. Anderson, *J. Electrochem. Soc.* **2019**, *166*, F282.
[40] Y. Dong, Y. Wu, M. Liu, J. Li, *ChemSusChem* **2013**, *6*, 2016–2021.
[41] H. Guo, Z. Fang, H. Li, D. Fernandez, G. Henkelman, S. M. Humphrey, G. Yu, *ACS Nano* **2019**, *13*, 13225–13234.
[42] C. Luo, Y. Zhang, X. Zeng, Y. Zeng, Y. Wang, *J. Colloid Interface Sci.* **2005**, *288*, 444–448.
[43] H. Jang, J. H. Lee, J. R. Lee, T. W. Kim, *ACS Appl. Energ. Mater.* **2022**, *5*, 9297–9302.
[44] Y. Liao, J. Xiang, L. Yuan, Z. Hao, J. Gu, X. Chen, Y. Huang, *ACS Appl. Mater. Interfaces* **2018**, *10*, 37955–37962.
[45] C. Yang, H. Wang, S. Lu, C. Wu, Y. Liu, Q. Tan, Y. Xiang, *Electrochim. Acta* **2015**, *182*, 834–840.
[46] L. Braic, N. Vasilantonakis, A. Mihai, I. J. Villar Garcia, S. Fearn, B. Zou, N. M. Alford, B. Doiron, R. F. Oulton, S. A. Maier, A. V. Zayats, P. K. Petrov, *ACS Appl. Mater. Interfaces* **2017**, *9*, 29857–29862.
[47] G. Greczynski, S. Mráz, L. Hultman, J. M. Schneider, *Appl. Phys. Lett.* **2016**, *108*, 041603.
[48] Z. Oktay, Z. Kahraman, M. Urgen, K. Kazmanli, *Appl. Surf. Sci.* **2015**, *328*, 255–261.
[49] Z. Cui, C. Zu, W. Zhou, A. Manthiram, J. B. Goodenough, *Adv. Mater.* **2016**, *28*, 6926–6931.
[50] D. Zhao, Z. Cui, S. Wang, J. Qin, M. Cao, *J. Mater. Chem. A* **2016**, *4*, 7914–7923.
[51] H. Xiao, C. Jia, B. Liu, Y. Huang, W. Cai, J. Li, Y. Huang, *J. Am. Chem. Soc.* **2019**, *141*, 3014–3023.
[52] V. Pfeifer, T. E. Jones, J. J. Velasco Velez, R. Arrigo, S. Piccinin, M. Havecker, R. Schlögl, *Chem. Sci.* **2017**, *8*, 2143–2149.
[53] M. Chourashiya, R. Sharma, S. M. Andersen, *Anal. Chem.* **2018**, *90*, 14181–14187.

Manuscript received: November 26, 2022
Revised manuscript received: December 21, 2022
Accepted manuscript online: January 3, 2023
Version of record online: January 13, 2023